



Probabilistic guidance for catheter tip motion in cardiac ablation procedures



Mihaela AM Constantinescu^a, Su-Lin Lee^a, Sabine Ernst^b, Apit Hemakom^c, Danilo Mandic^c, Guang-Zhong Yang^{a,*}

^aThe Hamlyn Centre for Robotic Surgery, Imperial College London, London SW7 2AZ, UK

^bRoyal Brompton Hospital, London SW3 6NP, UK

^cCommunications and Signal Processing group, Department of Electrical and Electronic Engineering, Imperial College London, London SW7 2AZ, UK

ARTICLE INFO

Article history:

Received 16 February 2017

Revised 12 March 2018

Accepted 20 March 2018

Available online 23 March 2018

Keywords:

Cardiac ablation

Intraoperative guidance

Catheter motion

Probabilistic map

Multivariate empirical mode decomposition (MEMD)

ABSTRACT

Radiofrequency catheter ablation is one of the commonly available therapeutic methods for patients suffering from cardiac arrhythmias. The prerequisite of successful ablation is sufficient energy delivery at the target site. However, cardiac and respiratory motion, coupled with endocardial irregularities, can cause catheter drift and dispersion of the radiofrequency energy, thus prolonging procedure time, damaging adjacent tissue, and leading to electrical reconnection of temporarily ablated regions. Therefore, positional accuracy and stability of the catheter tip during energy delivery is of great importance for the outcome of the procedure. This paper presents an analytical scheme for assessing catheter tip stability, whereby a sequence of catheter tip motion recorded at sparse locations on the endocardium is decomposed. The spatial sliding component along the endocardial wall is extracted from the recording and maximal slippage and its associated probability are computed at each mapping point. Finally, a global map is generated, allowing the assessment of potential areas that are compromised by tip slippage. The proposed framework was applied to 40 retrospective studies of congenital heart disease patients and further validated on phantom data and simulations. The results show a good correlation with other intraoperative factors, such as catheter tip contact force amplitude and orientation, and with clinically documented anatomical areas of high catheter tip instability.

Crown Copyright © 2018 Published by Elsevier B.V. All rights reserved.

1. Introduction

Heart rhythm disorders are serious conditions affecting the cardiac contraction and output, which can lead to stroke and sudden death. Worldwide, 33.5 million people suffer from atrial fibrillation, with additional patients presenting with atrial and ventricular tachycardias, atrial flutter and other arrhythmias (Chugh et al., 2014). Rhythm disorders are poorly tolerated in particular by patients with congenital heart disease (CHD), such as Tetralogy of Fallot or univentricular hearts treated by Fontan procedure. In these patients, the right ventricle has numerous scars after surgery and the right atrium haemodynamics are often distorted by a baffle (total cavopulmonary connection). Therefore, such patients are more

prone to life-threatening arrhythmias (Ernst et al., 2012). Because of their pre-existing cardiac structural abnormality, scarred myocardial incisions, and abnormal blood flow patterns, the CHD cohort is deemed one of the most challenging patient groups when it comes to the management of heart rhythm disorders (Roy et al., 2016).

Radiofrequency catheter ablation is one of the established curative methods for cardiac arrhythmias. It consists of focal delivery of radiofrequency energy from the tip of a catheter introduced endovascularly and placed in contact with the endocardium. Most commonly, the ablation is performed during the arrhythmia in order to target the correct site. However, for CHD patients who cannot sustain stable haemodynamics, many procedures have to be performed under sinus rhythm (Roy et al., 2016), i.e., cardiac cycle length between 600 and 1000 ms.

Despite its recognised merits, radiofrequency ablation still has a relatively low success rate, with 80% suggested for atrial fibrillation after an average of 1.3 procedures per patient (Cappato et al., 2010). The main causes of failure and need for repeat ablation are

* Corresponding author.

E-mail addresses: mihaela.constantinescu12@imperial.ac.uk (M.A. Constantinescu), su-lin.lee@imperial.ac.uk (S.-L. Lee), S.Ernst@rbht.nhs.uk (S. Ernst), apit.hemakom12@imperial.ac.uk (A. Hemakom), d.mandic@imperial.ac.uk (D. Mandic), g.z.yang@imperial.ac.uk (G.-Z. Yang).

insufficient energy delivery to targeted tissue and incorrect localisation, both of which can be traced back to the instability of the catheter tip positioning on the endocardium.

While CHD patients are indeed a very challenging cohort for arrhythmia treatment, the concerns related to catheter tip stability are of primary importance in all radiofrequency ablation procedures, irrespective of the patient group. For procedures such as focal ablation of single arrhythmia sources, the need for catheter tip position accuracy is paramount, but it is also an important factor in circular isolation of pulmonary veins for treatment of atrial fibrillation and in linear transection of macro-reentrant tachycardia circuits. This is because both procedures are performed as a series of closely positioned point-wise ablations. Several clinical studies analysed the continuity of ablations produced by different operators during pulmonary vein isolation in left atria and it was concluded that the pulmonary vein ostiae were among the most challenging anatomical locations to ablate (Neuzil et al., 2013; Maki-moto et al., 2014).

Two notable developments are currently employed by the interventionist in order to improve guidance at the ablation site: electroanatomical mapping and contact force sensors. Electroanatomical mapping systems such as CARTO (Biosense Webster, Diamond Bar, CA, USA) or EnSite (St Jude Medical, St Paul, MN, USA) enable real-time tracking of the catheter tip in an electromagnetic field and subsequent building of the anatomy by spatially interpolating the positions at which the catheter touches the endocardium. Simultaneous electrical data, such as electrogram voltages, local time activation, and impedance, are overlaid on the reconstructed anatomy as colour maps. At the advent of cardiac ablation, clinicians guided their catheter positioning by the consistency of electrogram amplitudes at sites of good contact (Squara et al., 2014). However, electrical values change after ablation, rendering the method unreliable during the energy delivery itself.

Recent-generation catheters such as the THERMOCOOL (Biosense Webster, Diamond Bar, CA, USA) or the TactiCath (St Jude Medical, St Paul, MN, USA) incorporate contact force sensors at the tip. Contact force has become a measure of catheter stability and the force-time integral an estimation of the lesion quality. However, Shah and Namdar (2015) were among the first to acknowledge the possibility of catheter tip sliding under consistent amplitude of the contact force, which they defined as spatial instability. The authors distinguished between spatial stability, quantified by the sliding distance, and temporal stability, measured by contact force amplitude and force-time integral, concluding that force amplitude information alone was not a measure of good contact.

The catheter tip trajectory is a summation of the respiratory and cardiac motions of the chamber wall at the catheter contact point and of a third component of tip slippage along the endocardium. This third component has been neglected in stability studies so far, with most of the analysis driven by compensating respiration in intraoperative data. For example, the oscillatory motion of the catheter was gated in order to improve the electroanatomical mapping, assuming that the largest component influencing the map accuracy was the respiration (Klemm et al., 2007). Ignoring the other signal components caused an error comparable to the amplitude of the respiratory motion itself, thus limiting the applicability of the method.

While respiratory gating has become an available option in electroanatomical mapping systems, efforts have been made to correct fluoroscopy images used as alternative guidance for the same type of cardiac procedures. This was achieved by tracking either the diaphragm or the reference catheters, such as the one in the coronary sinus, in a series of fluoroscopic images (King et al., 2009; Sundar et al., 2009; Ma et al., 2010; Panayiotou et al., 2012). The motion was decomposed either using bandpass filters or Principal

Component Analysis (PCA), whereby it was assumed that the signal contained only oscillatory components of cardiac and respiratory motion, thus ignoring any spatial drift which none of the methods would be able to capture.

As an increasing number of procedures involve the use of electroanatomical maps and electromagnetically tracked catheters, the tip position recordings have also been analysed. Electroanatomical mapping systems enable the tracking and the export of the catheter tip position at each sparse mapping point for 2.5 s. This acquisition window length is a setting of the electroanatomical mapping system and allows for endocardial position synchronisation for all mapping points to the same cardiac phase. Bandpass filtering was applied to these positional signals in order to recover cardiac and/or respiratory motion (Porrás et al., 2013; Roujol et al., 2013). The frequency of the cardiac passband was computed from the electrocardiogram (ECG), while the unknown respiratory rate was approximated to the average healthy subject rate of 18 breaths/min (Roujol et al., 2013). However, the 2.5 s-long signal contained only a small number of oscillations, which affected the bandpass filter robustness in accurately recovering the components.

Independent Component Analysis (ICA) (Hyvaerinen and Oja, 2000) is a source separation method commonly applied to superimposed signals. With bandpass filtering requiring a high oscillatory content in the analysed signal, PCA only being able to decompose oscillatory components similar in all directions, and ICA assuming statistically independent components, there is a need for an adaptive, data-driven decomposition method. Multivariate Empirical Mode Decomposition (MEMD) (Rehman and Mandic, 2010; Mandic et al., 2013) was applied with better results than the other methods (Constantinescu et al., 2015). The method is an iterative process through which an intrinsic mode function (IMF) is extracted at each step using the so-called sifting process. The sifting process repeatedly removes a local mean from each sifting input of a given multivariate signal, which results in a set of IMFs in descending order of their frequency.

In this paper, a catheter ablation guidance framework is presented based on the extraction of the motion components in the electromagnetically tracked catheter tip position signal using MEMD. Aside from the cardiac and respiratory components well documented in previous work, the focus of the decomposition results is a third previously unaccounted for component, the sliding motion along the endocardium. The drift during a fixed frame of 2.5 s is quantified and the maximal slippage for each mapping point is computed. Simultaneously, the IMFs are fed into a Dynamic Bayesian Network (DBN) parameterised for each mapping point, modelling the dependencies of cardiac, respiratory and drift motion from one time point to the next. Finally, the conditional probability of the maximal slippage is computed from a multivariate normal regression model and overlaid on the electroanatomical map. A complete anatomy-specific probabilistic map of slippage is generated from all available mapping points. The key steps of the analysis flow are illustrated in Fig. 1. In order to assess the efficacy of the method, the proposed framework was tested on 40 electrophysiology studies of CHD patients and additional prospective validation was performed on phantom and simulated data.

The present work is an extension of (Constantinescu et al., 2015), with significant changes and adaptations in the decomposition algorithm. It also eliminates the use of a Gaussian mixture model fit in the computation of slippage probabilities, thus deeming the probabilistic method more generalisable to non-Gaussian slippage components. Furthermore, the new method was validated on 40 patients, supported by detailed simulation and phantom experiments.

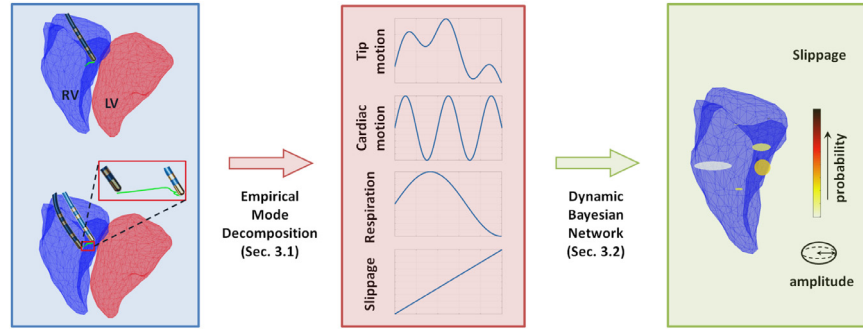


Fig. 1. Catheter tip stability is a major concern in radiofrequency ablation of cardiac arrhythmias. Both cardiac and respiratory motion can cause catheter tip movement. In this paper, we account for an additional motion component, i.e., catheter tip slippage along the endocardium. A novel multivariate approach to EMD is used to extract the three components and the slippage is modelled in a DBN to compute the probability of the maximal slippage value at each sparsely sampled mapping point.

2. Materials and methods

2.1. Catheter tip motion decomposition

The catheter tip motion is a superimposition of three types of motion: two oscillatory components of cardiac contraction and respiration and a monotonic endocardial slippage component. Moreover, each constitutive signal is represented by its 3D components. The extraction of the three physiological signals in each direction poses a challenge often encountered in biomedical signal processing and solved commonly through spectral windowing or Blind Signal Separation. Spectral windowing is based on frequency domain analysis, whose accuracy depends on the oscillatory content of the mixed signal. In turn, Blind Signal Separation techniques, such as ICA or PCA, rely on statistical independence properties of the signal components. The performance of these methods is limited if the assumptions are not met, as is the case of the short catheter tip motion recordings and the highly dependent respiratory and cardiac signals. An alternative approach is (Multivariate) Empirical Mode Decomposition ((M)EMD), which uses the local instantaneous frequency and amplitude of the signal at each time stamp, thus better accommodating the physiological signal than spectral filtering, while also not forcing statistically independent components.

2.1.1. Multivariate empirical mode decomposition (MEMD)

MEMD can be used to extract the cardiac motion, respiration, and slippage from the superimposed Cartesian position signal \mathbf{x} of the catheter tip as in Eq. (1), where M is the number of oscillatory components (IMFs), N the number of samples, P the number of channels in the multivariate signal, i.e., 3 for the Cartesian position; $\mathbf{a}_{m,k}$ is the amplitude value which modulates the underlying oscillation Ψ_m of the m -th IMF at time stamp k , and \mathbf{r} is the residual trend vector for each channel. The multivariate channels were projected along specified directions in order to ensure the same number of IMFs in all channels and the same frequency and amplitude range for the IMFs of the same order. The extrema at each iteration were computed in the projection space and then interpolated in order to obtain meaningful envelopes in the original space (Algorithm 1).

$$\mathbf{x}_{i,k} = \sum_{m=1}^M \mathbf{a}_{m,k} \Psi_{m,k} + \mathbf{r}_k, \quad i = \overline{1, P}; \quad k = \overline{1, N} \quad (1)$$

2.1.2. Noise-Assisted (NA)-MEMD

Despite the capability of MEMD in extracting physically meaningful components, mode-splitting, i.e., one of the physiological signals being divided among more than one IMF of the same frequency, can occur. This is caused by the sub-Nyquist

Algorithm 1: Pseudo-code of the MEMD algorithm (Rehman and Mandic, 2010; Mandic et al., 2013).

Data: $\mathbf{x}(t) = [x_1(t) \ x_2(t) \ \dots \ x_P(t)]$ multivariate signal of P channels.

Result: IMFs

while $\mathbf{x}(t)$ is not a monotonic function (residual) **do**

while no valid IMF **do**

1. Generate Q uniformly sampled points on a $(P-1)$ -dimensional sphere using the Hammersley sequence.
 2. Establish Q direction vectors \mathbf{v}_q , $q = \overline{1, Q}$.
 3. Compute the projections $\mathbf{w}_q(t)$.
 4. Find the time stamps t_e in $\mathbf{w}_q(t)$ which represent extrema locations in all of its components.
 5. Compute the correspondent extrema in the original multivariate signal $\mathbf{x}(t_e)$.
 6. Interpolate the multivariate extrema to construct the multivariate minima and maxima envelope curves $\mathbf{x}_{\min}(t)$ and $\mathbf{x}_{\max}(t)$.
 7. Calculate the local mean $\mathbf{x}_{\text{avg}}(t) = \frac{\mathbf{x}_{\min}(t) + \mathbf{x}_{\max}(t)}{2}$.
 8. Subtract $\mathbf{x}_{\text{avg}}(t)$ for the potential IMF at this iteration $\mathbf{d}(t) = \mathbf{x}(t) - \mathbf{x}_{\text{avg}}(t)$.
- if** $\mathbf{d}(t)$ has a mean close to zero and the number of zero crossings and extrema differ by at most one **then**
- $\mathbf{d}(t)$ is an IMF.
 - $\mathbf{x}(t) = \mathbf{x}(t) - \mathbf{d}(t)$.
- else**
- $\mathbf{x}(t) = \mathbf{d}(t)$.

sampling of local extrema and thus the aliasing IMF spectra. Ur Rehman et al. (2013) suggested the addition of noise channels in as high a number as possible, in order to cancel out the effect of the artificial input. A high enough number of noise channels not only ensures a uniform population in the frequency spectrum, but also little dependency among the input channels, resulting in better decomposition (Looney et al., 2015). The subsequent Noise-Assisted (NA)-MEMD method decomposed a $m + n_{\text{WGN}}$ multivariate signal and retained only the first m IMFs, where m is the order of the original multivariate signal and n_{WGN} is the number of white Gaussian noise channels. However, the computational costs of NA-MEMD increase with the number of noise channels and an analysis on the optimal number should be performed.

2.1.3. Adaptive-projection intrinsically transformed (APIT)-MEMD

The multivariate input is a superposition of signals of different power. Moreover, with the addition of a limited and not infinite

number of noise signals, the inter-channel correlation increases. Both of these aspects may adversely influence the decomposition. Theoretically, this problem can be alleviated with a high number of uniformly sampled projection vectors, but the computational costs do not justify the solution. Instead, the computation of adaptive projection directions at each iteration in the MEMD sifting was proposed, leading to Adaptive-Projection Intrinsically Transformed (APIT)-MEMD (Hemakom et al., 2016).

The Hammersley uniform sampling is preceded by a stage of PCA which computes the first eigenvector as the direction of the power imbalance among potential signal components, e.g. respiratory vs. cardiac motion. The direction vectors generated using the Hammersley sequence are then redirected towards the first principal component eigenvector by a factor α . The direction vectors become $\hat{\mathbf{v}}_q = \frac{\mathbf{v}_q + \alpha\sigma}{|\mathbf{v}_q + \alpha\sigma|}$, where σ is the eigenvector of the first principal component (Algorithm 2).

Algorithm 2: Pseudo-code of the APIT-MEMD algorithm (Hemakom et al., 2016).

Data: $\mathbf{x}(t) = [x_1(t) \ x_2(t) \ \dots \ x_p(t)]$ multivariate signal of P channels.

Result: IMFs

while $\mathbf{x}(t)$ is not a monotonic function (residual) **do**

while no valid IMF **do**

1. Apply PCA on the multivariate signal $\mathbf{x}(t)$ and retain the first eigenvector σ as the principal direction of power imbalance among the channels.
2. Perform steps 1 and 2 of MEMD in Alg. 1. **if**
3. Relocate the direction vectors using $\hat{\mathbf{v}}_q = \frac{\mathbf{v}_q + \alpha\sigma}{|\mathbf{v}_q + \alpha\sigma|}$, with $\alpha \in (0,1)$.
4. Perform steps 3–7 of MEMD in Alg. 1.

if $\mathbf{d}(t)$ has a mean close to zero and the number of zero crossings and extrema differ by at most one **then**

$\mathbf{d}(t)$ is an IMF.
 $\mathbf{x}(t) = \mathbf{x}(t) - \mathbf{d}(t)$.

else

$\mathbf{x}(t) = \mathbf{d}(t)$.

2.1.4. Extraction of cardiac, respiratory and slippage components

For each sequence of tip position recordings, noise-assisted APIT-MEMD was applied. Due to the computation of the IMFs as average of the envelope signals, the MEMD algorithms provided an intrinsic sorting of the IMFs by their instantaneous frequency, e.g. from the highest frequency of noise to the lowest frequency, e.g. the trend. This feature was used in the identification of the cardiac, respiratory and slippage components in each set of decomposed IMFs.

Firstly, the selection of the cardiac component was performed. The use of the noise-assisted method ensured that no mode-splitting occurs. Therefore, given the exact heart rate from the ECG, a single component was sought, i.e., the one with the periodicity closest to the ECG. The periodicity was quantified by the average of all N instantaneous frequencies, whereby N is the length of the position recording.

Secondly, the respiratory and slippage components were estimated. Unlike the cardiac motion, there was no ground truth for the respiratory rate and also the CARTO signal is too short for a precise estimate. Therefore, a window of 12–40 strokes/min, the common physiological range of respiratory frequency variation, was defined; all IMFs of frequency within the defined range were summed into one respiratory component. The same procedure

was performed for all remaining IMFs of frequency lower than 12 min^{-1} , which were summed into the slippage.

2.2. Probabilistic slippage prediction

The time series of the recorded catheter tip signal and of the extracted components were modelled in a DBN (Fig. 2), where each time stamp had corresponding values of instantaneous cardiac C_k , respiratory R_k and slippage S_k motion amplitudes, as well as the measured value of the cumulated motion T_k . The conditional probability of slippage $P(S_k | C_{k...1}, R_{k...1}, T_{k...1})$ describing the occurrence of a drift value S_k at time stamp k was computed from a multivariate normal regression model parameterised with the predictors $C_{k...1}$, $R_{k...1}$, $T_{k...1}$, which are the extracted location-specific components. The regression model can be described by Eq. (2), with β_s the matrix of regression coefficients. The response vector \mathbf{S} is the amplitude of slippage at each time point, computed from its Cartesian components. The tip position \mathbf{T} is included in the predictor matrix as its 3D components \mathbf{T}_x , \mathbf{T}_y , and \mathbf{T}_z , while \mathbf{C}_x , \mathbf{C}_y , \mathbf{C}_z and \mathbf{R}_x , \mathbf{R}_y , \mathbf{R}_z are the Cartesian components of the APIT-MEMD decomposed cardiac and respiratory motion, respectively.

$$\mathbf{S} = [\mathbf{C}_x \ \mathbf{C}_y \ \mathbf{C}_z \ \mathbf{R}_x \ \mathbf{R}_y \ \mathbf{R}_z \ \mathbf{T}_x \ \mathbf{T}_y \ \mathbf{T}_z] \beta_s + \mathbf{e}_s \quad (2)$$

The multivariate normal regression model imposed the regression error \mathbf{e}_s to be normally distributed with mean 0, allowing for the probabilities of each error $\mathbf{e}_{s,k}$, $k = 1, N$, N being number of samples in the signal, to be computed from the normal distribution itself. Furthermore, it was assumed that if a slippage value fitted the regression model accurately, i.e., it could be predicted, its error would be small and the probability would be high. Thus, one-to-one mapping of the error probability on the slippage probability could be performed. Finally, the maximal slippage in the time series and its corresponding probability could be extracted for each mapping point.

2.3. Catheter tip motion estimation

Based on the maximal slippage probability at each sampled point on the endocardium, a global stability map was generated. The slippage information was overlaid on the existing electroanatomical map. For each mapping point, an ellipsoid with the axial length equal to the slippage in that direction was created. The ellipsoids were colour-coded according to the slippage probability at a given mapping point.

2.4. Simulation data

Datasets of catheter tip movement were generated by superimposing periodic cardiac and respiratory motion and linear monotonic slippage of 2 mm/s. The heart rate, amplitude and phase of the cardiac motion were set as the median measured in the patient data, i.e., 64.62 beats/min, 1.09 mm, 0.54 mm, and 1.7 mm of motion amplitude, and -2.88 rad, 3.01 rad, and -0.03 rad of phase difference in each Cartesian direction, respectively).

The respiratory signal followed the mathematical expression in Eq. (3), adapted from (Lujan et al., 1999), with fixed amplitude A_r (4.3 mm, 3.5 mm, and 0.21 mm in each direction, medians of patient data) and fixed phase difference between channels ϕ (1.79 rad, 1.8 rad, and -3.87 rad as computed from the patient data).

$$R(t) = A_r(1 - 2 \cdot \sin^{2n}(2\pi f_r t + \phi)), \quad n = 3 \quad (3)$$

The respiratory rate f_r varied between 12 breaths/min and 40 breaths/min, the range of healthy human breathing, yielding in total 29 values. The phase difference between the respiratory wave and the cardiac wave, i.e., the time difference from the beginning

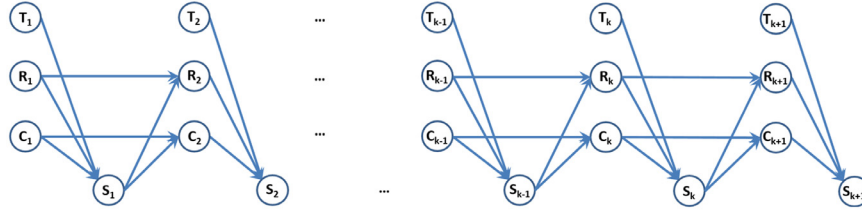


Fig. 2. DBN describing the transitions between consecutive states and the inter- and intra-state conditional dependencies. The cardiac (C_k) and respiratory (R_k) motion and the relative slippage (S_k) encode the values decomposed by the APIT-MEMD algorithm, while T_k is their summation at time stamp k . The values are also followed in subsequent time stamps as C_{k+1} , R_{k+1} , S_{k+1} and T_{k+1} .

of the simulation, was also varied between 0 and 99% of the respiratory period, generating in total 100 values. Thus, a grid of combinations of respiratory rates and phase differences was created for the cumulated signal. In total, 29×100 3D signals were decomposed. The added signal had the length of a regular CARTO mapping point recording of 2.5 s and was sampled at 1 kHz.

The choice of varying only the respiratory rate and the phase difference was motivated by their importance when decomposing a short signal. Firstly, it was hypothesised that a high respiratory rate interfered with the extraction of the cardiac signal. Secondly, a 2.5 s window of recording only allowed for an incomplete capture of the respiratory wave. Depending on the start of the window, i.e., phase difference, the captured sequence included the wave peak, in which case it was assumed that the signal decomposition will be more accurate, or only a linear section, which might cause the respiratory wave to be indistinguishable from the slippage.

2.5. Phantom data

A four-chamber cardiac phantom was 3D-printed in a PolyJet digital material mix of TangoPlus and VeroClear (shore durometer A50) on a Stratasys Objet500 Connex3 printer (Stratasys, Eden Prairie, MN, USA) from MRI images of a normal subject. The images were segmented by a clinician in the CARTO Segmentation Module (Biosense Webster, Diamond Bar, CA, USA) and then processed with MeshLab (Cignoni et al., 0000) and Meshmixer (Schmidt and Singh, 2010) to create the final STL file.

The two halves of the heart are completely separated, with the atria and the ventricles directly linked, without valves. The phantom's vascular connections were the superior and inferior venae cavae and the pulmonary artery on the right side and the left and right pulmonary veins and the aorta on the left side (Fig. 3(a)). For each of the right heart chambers, a soft balloon was molded to fit inside the RA and RV, respectively (Fig. 3(b)). The balloons were inserted into the phantom one at a time and inflated and deflated using a pump at a fixed rate of 60 beats/min, to mimic the contractile motion of the heart. The entire phantom was then placed on a translational motion rig powered by a linear motor (Faulhaber, Schoenaich, Germany). The rig (Fig. 3(c)) was designed to generate the diaphragmatic motion in Eq. (3), with maximal respiratory displacement of 20 mm ($A_r = 10$ mm) and fixed respiratory rate of 15 breaths/min ($f_r = 0.4$ Hz).

For the RA, the superior vena cava and the pulmonary artery were connected to the inlet and the outlet of the pump, respectively, whereas the inferior vena cava, with the balloon at atmospheric pressure, was used to insert the catheter (Fig. 3(d)). For the RV, the pump connections were the two venae cavae, while the pulmonary artery was used to access the chamber (Fig. 3(e)).

The superimposed signal was captured with an Aurora electromagnetic tracking device (NDI, Waterloo, Ontario, Canada) which recorded data from a 5-DOF catheter sensor at 40 Hz. The catheter was affixed to a single point on the balloon, simulating the mapping at one endocardial position, and then reattached at the next

position. The signal length for each point was 140 s: for the first 70 s, the catheter tip moved only under cardiac and respiratory influence, and the next 70 s, the catheter was additionally moved arbitrarily, in order to simulate the slippage (Fig. 4). In total, 15 points were recorded in the RA and 19 points in the RV.

2.6. Patient data

Forty retrospective electrophysiology studies of CHD patients were used to assess the proposed methods on real clinical data. The datasets were collected using a force-sensing NAVISTAR mapping and ablation catheter (Biosense Webster, Diamond Bar, CA, USA). The positions of the electromagnetic sensor, as well as those of four additional electrodes within 1.5 cm from the tip had been recorded in CARTO 3 at 60 Hz over 2.5 s for each 3D mapping point. The reference system was built by a second electromagnetically tracked catheter inserted into the coronary sinus, whose tip position was recorded simultaneously to the mapping catheter position. In addition to the sparse position recordings and their corresponding ECG, the bipolar voltages at each mapping point were exported for further correlation and validation of the cardiac motion. Moreover, the fast anatomical map of each study was exported in order to build the global probabilistic map in the last stage.

For each mapping point, the cardiac period was computed as the RR interval on the ECG. Any mapping points outside sinus rhythm were excluded from the dataset. According to the clinical literature, sustained arrhythmia is avoided in CHD patients and was deemed irrelevant for this application (Ernst et al., 2012).

The sinus rhythm filtering resulted in 723 mapping points from 40 electrophysiology studies, out of which 555 also had reference catheter recordings. The points had been collected in 19 right ventricles (RV), 11 right atria (RA), 5 left atria (LA), 4 total cavopulmonary connection (TCPC), 1 left superior pulmonary vein.

Additional contact force amplitude and orientation relative to the catheter shaft had been recorded simultaneously to the catheter position for 110 of the 555 mapping points. The 3D contact force was decomposed along the Cartesian directions according to Eq. (4),

$$\mathbf{F}_{\text{global}} = \frac{\mathbf{O} \cdot \mathbf{F}_{\text{local}}}{|\mathbf{O}|}, \quad (4)$$

where $\mathbf{O} = [\mathbf{E}_x - \mathbf{T}_x, \mathbf{E}_y - \mathbf{T}_y, \mathbf{E}_z - \mathbf{T}_z]^T$ is the orientation of the catheter tip given by the tip coordinates $[\mathbf{T}_x \ \mathbf{T}_y \ \mathbf{T}_z]^T$ and the coordinates of the next electrode on the catheter shaft $[\mathbf{E}_x \ \mathbf{E}_y \ \mathbf{E}_z]^T$.

Moreover, $\mathbf{F}_{\text{local}} = |F| \cdot [\sin(\alpha)\cos(\beta), \sin(\alpha)\sin(\beta), \cos(\alpha)]^T$ is the cylindrical coordinate representation of the force with respect to the catheter tip. The force amplitude $|F|$, as well as its axial and lateral angles compared to the catheter shaft, α and β , respectively, were exported from CARTO. Eq. (4) transformed the force values from the local to the global reference frame, in which the catheter tip slippage was computed. The product in this equation is the dot product which transforms the local axes into the global Cartesian axes. An example of catheter tip trajectory and a snapshot of the corresponding force orientation is shown in Fig. 5. The

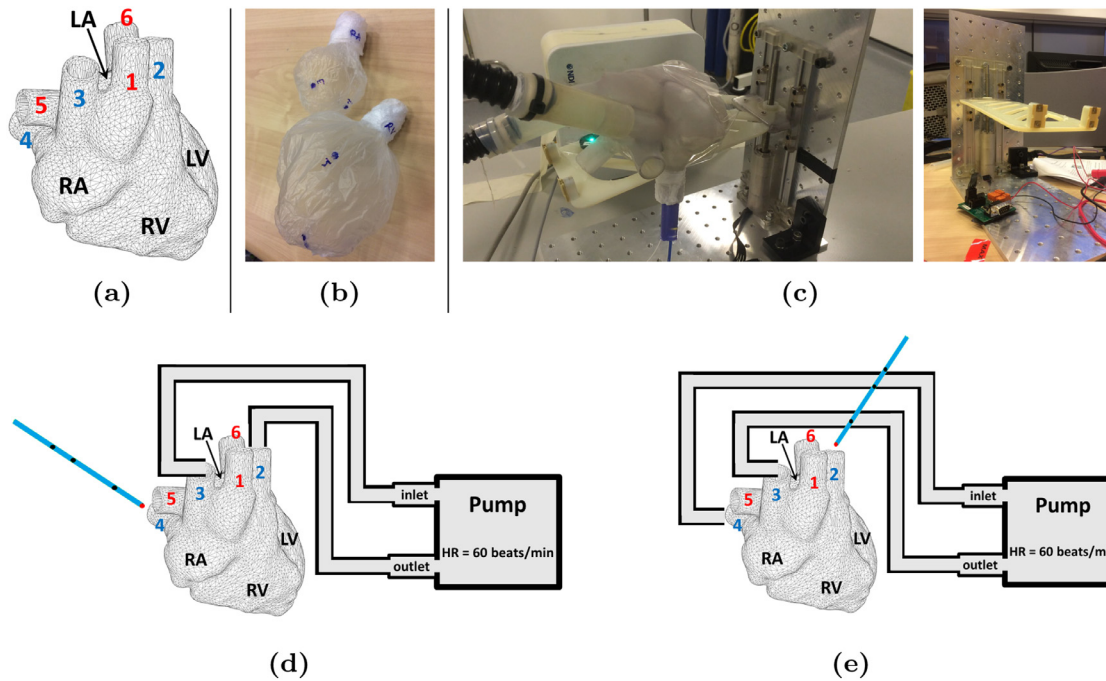


Fig. 3. (a) Surface model of the 3D-printed heart phantom. The blue in-/outlets belong to the right chambers and the red ones to the left. 1 – Aorta, 2 – Pulmonary artery, 3 – Superior vena cava, 4 – Inferior vena cava, 5 – Right pulmonary veins, 6 – Left pulmonary veins. (b) Inflatable balloons for the RA and the RV into which the catheter was inserted. The blue dots mark the targeted points. (c) Phantom experiment setup, with the respiratory motion rig simulating the diaphragm. (d) Pump connections and catheter insertion for RA experiments. (e) Pump connections and catheter insertion for RV experiments. (For interpretation of the references to colour in this figure legend, the reader is referred to the web version of this article.)

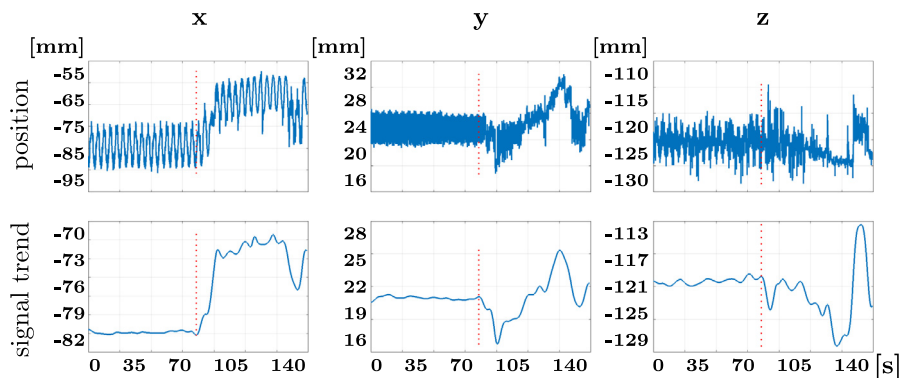


Fig. 4. Example of the 3D catheter tip motion for one point on the heart phantom. The first 70 s are taken under cardiac and respiratory motion only. The red dotted line shows the beginning of the slippage sequence. The first row shows the recorded sensor position and the second row shows the signal trend by which the onset of slippage was detected. (For interpretation of the references to colour in this figure legend, the reader is referred to the web version of this article.)

catheter force information was used to correlate and thus validate the slippage components in each Cartesian axis. A correlation coefficient between slippage and force amplitude was computed for each Cartesian direction. Finally, in order to correct for any bulk motion of the patient or for a potential drift of the reference catheter, which might have introduced an offset in the data, the reference catheter signal was subtracted from the mapping catheter recording.

3. Results

3.1. Catheter tip motion decomposition

3.1.1. Simulation results

Fig. 6 shows the decomposition results for a combination of 29 respiratory rates and 100 phase shifts of the respiratory wave. The cardiac signal recovery error increased three-fold between the respiratory rates of 35 breaths/min and 40 breaths/min (Fig. 6(a) and

(b)). On the other hand, the respiratory component was best recovered for 20 breaths/min to 35 breaths/min (Fig. 6(c)) due to a high number of oscillations in the recording window, but the extracted amplitude lacked in robustness, varying with the phase difference (Fig. 6(d)).

The median performance of APIT-MEMD was also compared with PCA and ICA applied on the 2.5 s-long simulated data. Fourier analysis on the short data was unable to recover the frequency spectrum required for bandpass filtering. The results for APIT-MEMD, PCA, and ICA are listed in Table 1. While the performance of all three methods on the respiratory wave was rather poor, the cardiac wave extraction results showed robustness of APIT-MEMD compared to PCA and ICA, which yielded very good results in frequency estimation, but failed in amplitude computation due to mode-mixing and the cardiac signal being split over all components.

Finally, the component of most interest was the slippage. The performance of the algorithms was quantified here by the correla-

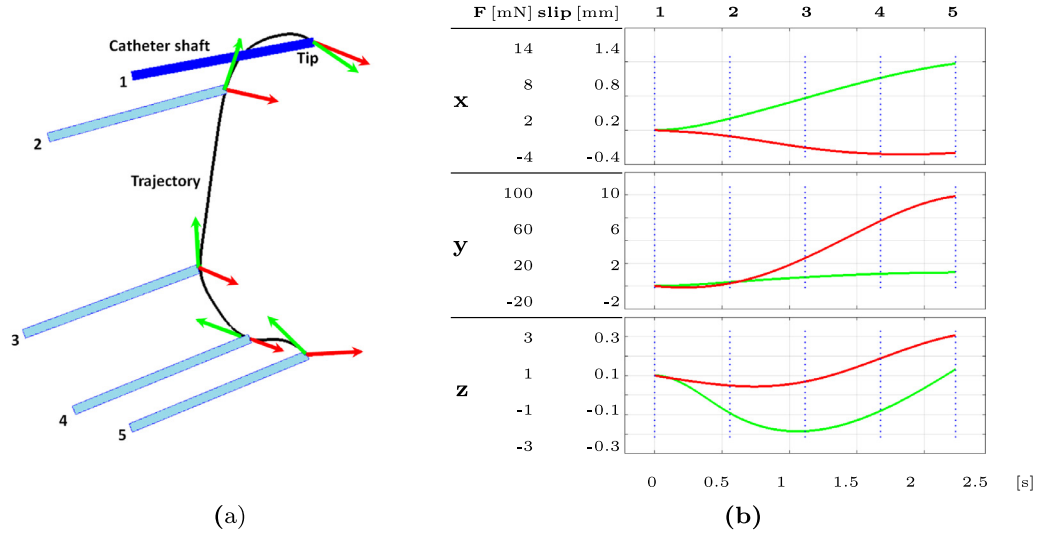


Fig. 5. (a) Example of force orientation (green), catheter tip (blue), tangential tip motion vector (red), and the catheter tip trajectory over an entire 2.5 s sequence (black). The five time points selected are also displayed as plots in (b). (For interpretation of the references to colour in this figure legend, the reader is referred to the web version of this article.)

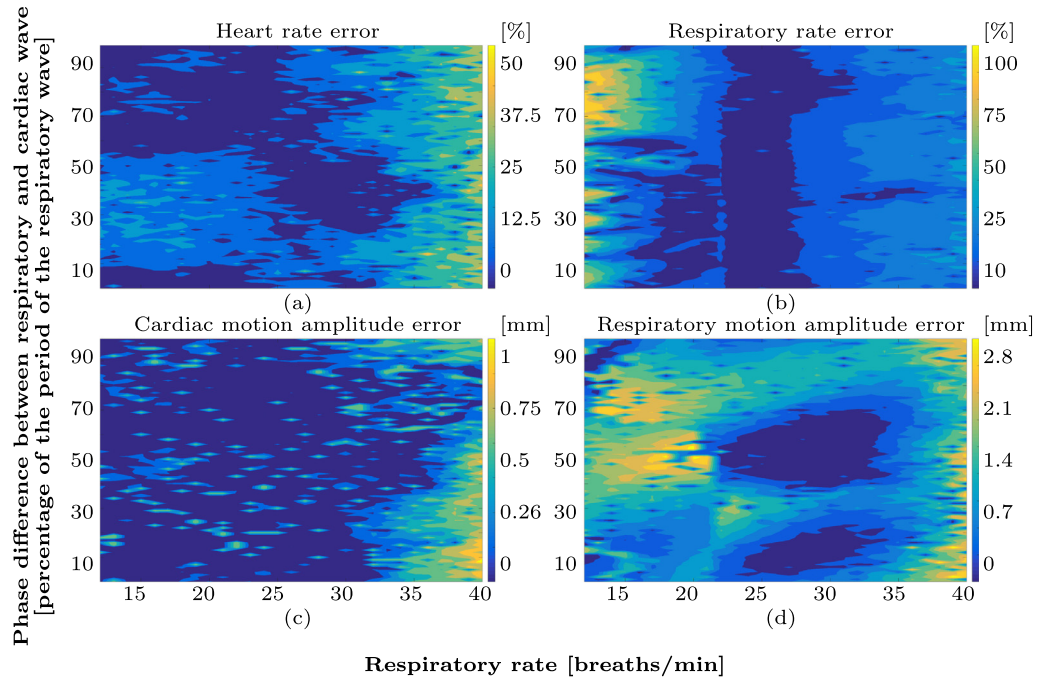


Fig. 6. Artificial signal decomposition results: (a,c) – cardiac motion; (b,d) – respiration. The decomposition accuracy worsened with increasing respiratory rate, due to overlaps with the cardiac spectrum. For respiratory rates under 20 breaths/min, the respiratory component was mistaken for the linear slippage due to insufficient oscillations in the 2.5 s simulation window.

Table 1

Comparison of cardiac and respiratory motion recovery errors as well as correlation coefficients between recovered and ground-truth slippage for APIT-MEMD, bandpass filtering, PCA, and ICA applied on the phantom and simulated data. N/A – not available.

		Cardiac motion [%]		Respiratory motion [%]		Slippage
		Frequency	Amplitude	Frequency	Amplitude	Corr. coeff.
simulations	APIT-MEMD	4.77	5.45	22.11	17.65	0.95
	bandpass	N/A	N/A	N/A	N/A	N/A
	PCA	0.74	86.61	19.39	20.41	0.02
	ICA	0.70	57.99	27.88	24.53	0.12
phantom	APIT-MEMD	8.57	30.28	36.73	48.91	0.68
	bandpass	1.33	570.13	6.97	77.02	0.51
	PCA	16.40	35.84	44.35	21.09	0.44
	ICA	16.02	37.34	37.34	24.16	0.44

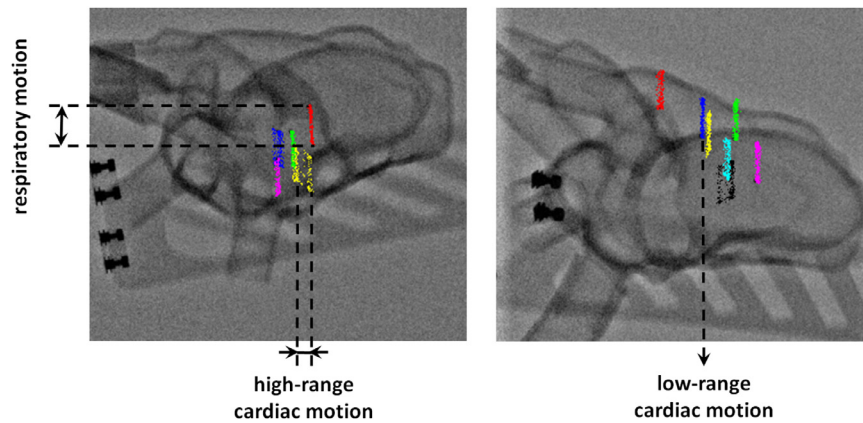


Fig. 7. X-ray images of the phantom experimental setup for point acquisitions in RA (left) and RV (right) with 5 recorded points in the RA and 7 in the RV. CT markers were placed at each point. The markers' movement is colour-coded and points of the same colour belong to the same marker, at different positions in time. The locations were segmented from 233 frames in the RA and 261 frames in the RV. The respiratory motion was unidimensional, following an oscillatory wave with amplitude 10 mm and frequency 15 breaths/min.

tion coefficient between the extracted signal and the ground truth. APIT-MEMD yielded the highest correlation coefficient among all algorithms, thus demonstrating its practical value for in vivo applications.

3.1.2. Phantom experiments

The moving heart phantom was scanned using cone-beam CT in an Innova 4100 (GE Healthcare, Chicago, IL, USA). Fig. 7 shows X-ray images in left-anterior-oblique view at 60° tilting of the C-arm. The left figure shows the range of motion of 5 CT markers in the RA, while the right figure shows 7 points in the RV. The position of the CT markers was segmented in 233 RA images and 261 RV images.

The controlled translational rig motion offered ground truth for the respiratory motion. Moreover, the phantom data of considerably longer recording time allowed for further validation of the proposed decomposition method. The additional validation data was extracted in the form of local cardiac and respiratory motion pattern by using a second-order bandpass filter calibrated at the known motion frequencies mimicking heart and diaphragm oscillations, i.e., 60 beat/min and 15 breaths/min. The application of frequency-based methods was possible due to the high oscillatory content in the 140 s recordings. Finally, the slippage component was the residual after subtraction of the previous two oscillations, calculated from the onset of the catheter manipulation as in Fig. 4. This process was performed for each of the 34 points individually.

Table 1 shows the comparative results of applying the proposed APIT-MEMD, bandpass filtering, PCA and ICA to the collected phantom data. The results are average values over the 34 datasets, whereby one dataset comprised of the first 2.5 s of catheter manipulation, in order to preserve the short-recording settings available in the CARTO system. Bandpass filtering generated the highest errors in motion amplitude recovery despite yielding the best frequency estimations. PCA and ICA performed similarly with adequate estimates of motion amplitude. Finally, APIT-MEMD yielded a good estimate of heart rate; however, it did encounter difficulties in estimating the parameters of respiratory motion because of the short signal.

The performance of slippage extraction was also quantified. The residual trend in Fig. 4 served as ground truth. APIT-MEMD again yielded the highest correlation coefficient between computed and ground truth slippage. Fig. 8(a) shows the slippage correlation values in each motion axis and Fig. 8(b) shows the mean slippage per second and the corresponding maximum slippage reached in each study. Moreover, an analysis over the ability of APIT-MEMD to

decompose the three different motion patterns was performed for varying signal acquisition lengths (Fig. 8(c) and (d)). While the cardiac motion does not benefit from the increasing window length (red curve – heart rate, green curve – amplitude), the respiratory motion estimation improves significantly with the window length, thus showing that the 2.5 s of signal acquisition are not optimal and should increase to at least 4 s, i.e., the period of respiratory motion chosen in these experiments. Additionally, the slippage correlation coefficient also increases with the length of the acquisition window, despite an outlier at 3 s. This increase is due to the better estimate of respiratory motion, which prevents its mixing with the slippage.

3.1.3. Patient data

Fig. 9 shows five 3D sequences of catheter tip position recordings in the RV and LA. The decomposition results are plotted underneath for comparison. It can be seen that the resulting components appear to be physiologically plausible. The cardiac signal has the periodicity of the ECG, with the respiratory wave and the slippage in decreasing order of frequency, the latter being close to a linear function.

The decomposition method was firstly quantified by the median error of heart rate recovery. The ground truth heart rate was extracted from the ECG at each mapping point. Fig. 10(a) shows the error histogram over all sampled points, with an emphasis on the 10% error threshold, below which APIT-MEMD performed in 59.09% of the cases, the 20% and 25%, around which three quarters of the points could be found, and the 33% threshold, which covered 92.25% of the cases. Moreover, Fig. 10(b) shows the quantile results and the computation time for a number of channels varying from 0 to 10. All algorithms were written in unoptimised Matlab R2016b and ran on an Intel i7 CPU at 3.4 GHz.

Secondly, the cardiac motion amplitude recovery was assessed. Due to the lack of ground truth, only a quantitative validation was performed. According to previously validated work (Roujol et al., 2013; Porras et al., 2013), contact points acquired in myocardial scar zones have a significantly lower cardiac motion amplitude than points in healthy tissue. This is due to the reduced contractility in pathological tissue. The cardiac motion amplitude extracted with the proposed method was grouped according to the bipolar voltage of the corresponding point. Scar points were defined as locations with bipolar voltage value lower than 0.5 mV, while the rest of the points were grouped into heterogeneous and healthy tissue, according to the standard for the right ventricle in clinical literature (Roujol et al., 2013). The two groups verified the previous

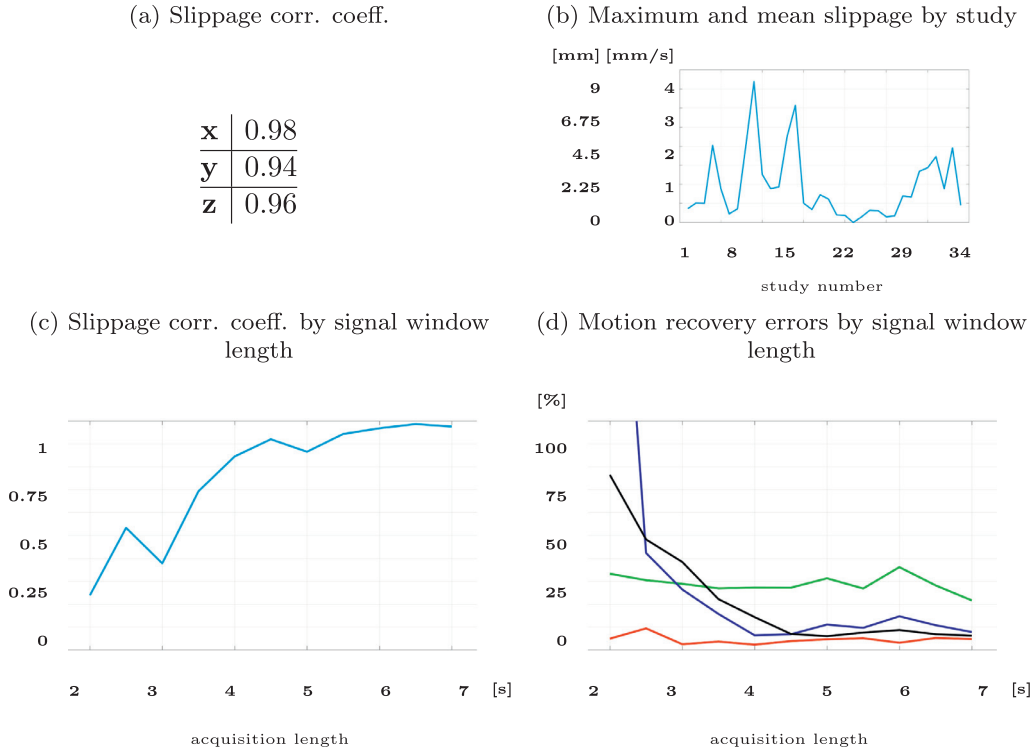


Fig. 8. Phantom experiments: (a) Slippage extraction performance in each direction by quantification of the correlation coefficient between ground truth slippage and extracted slippage. (b) Maximum and mean slippage in each phantom study. (c) Improvement in the correlation between computed slippage and ground truth slippage for increasing signal acquisition window. (d) Error reduction in the cardiac and respiratory motion with the increase of the signal acquisition window. Red – heart rate, green – heart motion amplitude, blue – respiratory rate, black – respiratory motion amplitude. (For interpretation of the references to colour in this figure legend, the reader is referred to the web version of this article.)

findings in (Roujol et al., 2013; Porras et al., 2013) with a statistically significant difference between them (Wilcoxon rank sum test, 5% significance level). There are no consistent guidelines for scar delineation in atria. Therefore, the cardiac motion amplitude analysis was performed on the RV data only.

For the validation of the slippage component, the 3D contact force was decomposed along the directions of slippage according to Eq. (4). There was a high correlation between the contact force and the slippage in each direction as can be seen in Fig. 11(a). According to (Shah and Namdar, 2015), force amplitude of under 196.13 mN (20 g) are indicative of instable contact. Moreover, the curves in Fig. 11(c) show the catheter slippage increasing with the force amplitude, proving the existence of catheter tip drift.

The maximal slippage was also assessed qualitatively. According to (Shah and Namdar, 2015), it is more difficult to keep a good contact with the more motion-prone ventricular wall than with the atrial wall. This results in more endocardial slippage in the ventricle than in the atrium. Along these lines, the maximal value of slippage over the entire signal length was compared for atrial and ventricular electrophysiology studies. The values decomposed with the proposed APIT-MEMD were in accordance with the clinical literature, independently of the chosen numbers of noise channels. Fig. 12 shows the average maximal slippage over all ventricular and atrial mapping points for a variable number of noise channels in APIT-MEMD.

3.2. Probabilistic slippage prediction and catheter tip motion estimation

The multivariate normal regression model in Eq. (2) was applied to the retrospective patient data in order to compute the probability of maximal slippage at each mapping point. The model was

cross-validated in a 90%–10% configuration, whereby 90% of the data was assigned to the training set and 10% was defined as the test set. This validation was performed for each of the 555 points 10 times, with the 10% test set as a sliding window through the entire dataset of the signal time series. The mean average for all 555 points are plotted in the histogram of Fig. 13, showing a narrow histogram of mode errors of the proposed regression model.

Following the validation of the underlying regression model which computes the local slippage probabilities, the global slippage maps were generated. Table 2 shows four probabilistic maps of slippage for RV, RA, LA, and TCPC, respectively, each with the median and maximal slippage values and their probabilities. It was noticed that the area around the tricuspid valve directing the flow from the RA to the RV, as well as the RV apex, were regions of high slippage probability. In the LA, unstable areas were the pulmonary veins ostiae, in accordance with the clinical literature (Neuzil et al., 2013; Makimoto et al., 2014).

4. Discussion

Catheter tip contact with endocardial tissue during cardiac ablation has been a major clinical concern. Existing literature recommends an empirical value of 196.12 mN (20 g) of contact force in order to ensure catheter tip stability (Shah and Namdar, 2015). This value is believed to show sufficient embedding of the catheter tip into the tissue so that sliding along the endocardium is minimised. However, it is also acknowledged that these guidance values cannot be met in all cases due to high perforation risk in thinner wall areas, such as the right side of the heart (Shah and Namdar, 2015) or in enlarged atria such as in CHD patients. In the datasets used in the present paper, the contact force amplitude was 164.75 ± 203.38 mN, which emphasised the need for an ad-

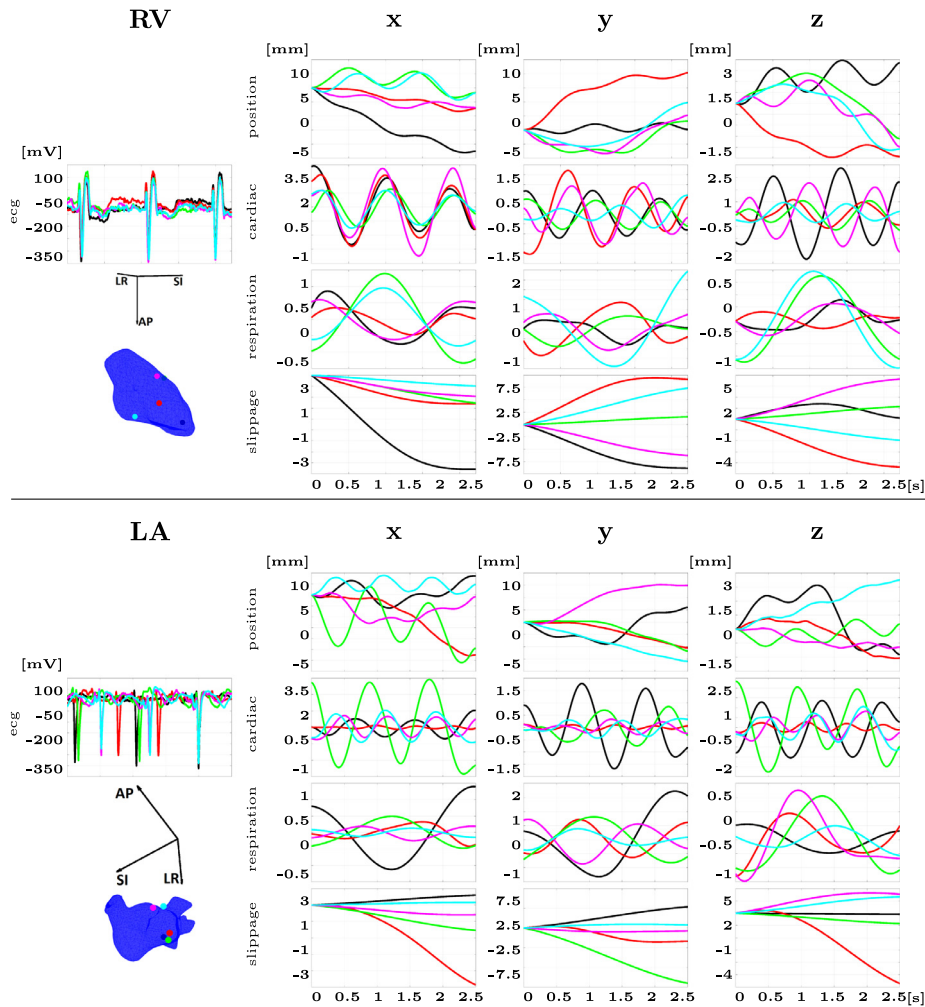


Fig. 9. APIT-MEMD decomposition results for five points in an RV and an LA. The orientation of the mesh is defined by the left-right axis (LR), superior-inferior axis (SI), anterior-posterior axis (AP). The upper row time series are the cumulated 3D signals shifted at a mutual origin of the five points. The remaining rows describe the components of interest in decreasing order of frequency: cardiac and respiratory motion and monotonic drift.

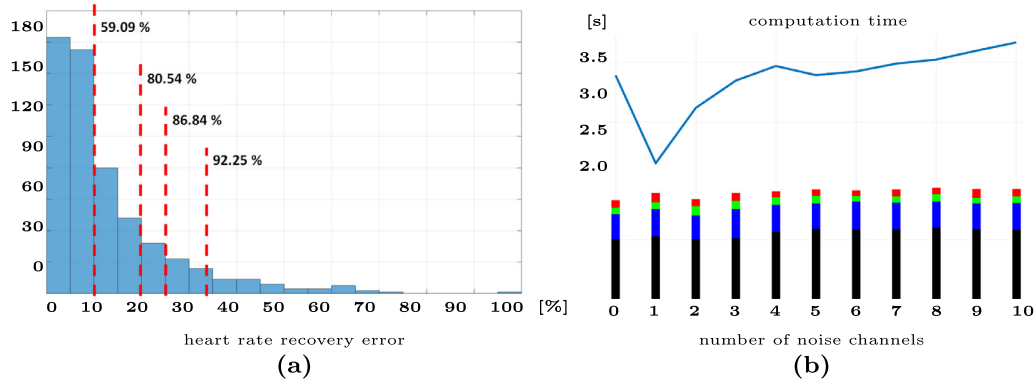


Fig. 10. (a) Histogram of heart rate errors over all 555 mapping points. For 59.09% of all points, the error was under 10%, for 80.54% of the points it was under 20%, for 86.84% it was 25%, and for 92.25% it was 33%. (b) APIT-MEMD computation time (top) and heart rate recovery error (bottom) dependency on the number of noise channels. The top of the bars represent the number of points within a certain threshold of error: black – 10% threshold, blue – 20%, green – 25%, red – 33%. The histogram in (a) is the detailed visualisation for 5 noise channels. (For interpretation of the references to colour in this figure legend, the reader is referred to the web version of this article.)

ditional analysis of the slippage itself, since the contact force amplitude was below the recommended threshold.

In this paper, a novel intraoperative guidance framework based on ablation catheter motion was proposed. Firstly, the 3D catheter tip position signal was decomposed into cardiac and respiratory oscillations and an additional unquantified sliding over the endo-

cardium which has been previously mentioned in the literature. Secondly, the maximal value of the sliding signal over time was computed for each point sampled on the anatomy. Finally, the probability of this maximal drift was estimated and displayed as a location-specific measure on the endocardial surface.

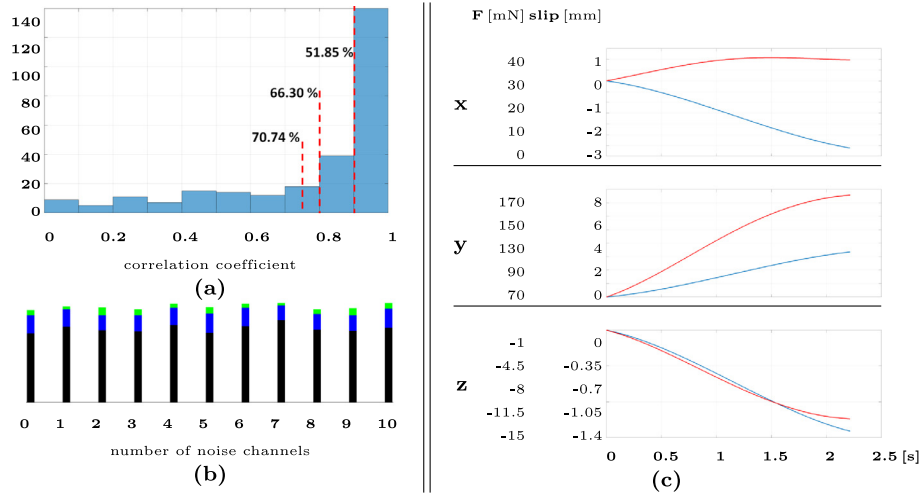
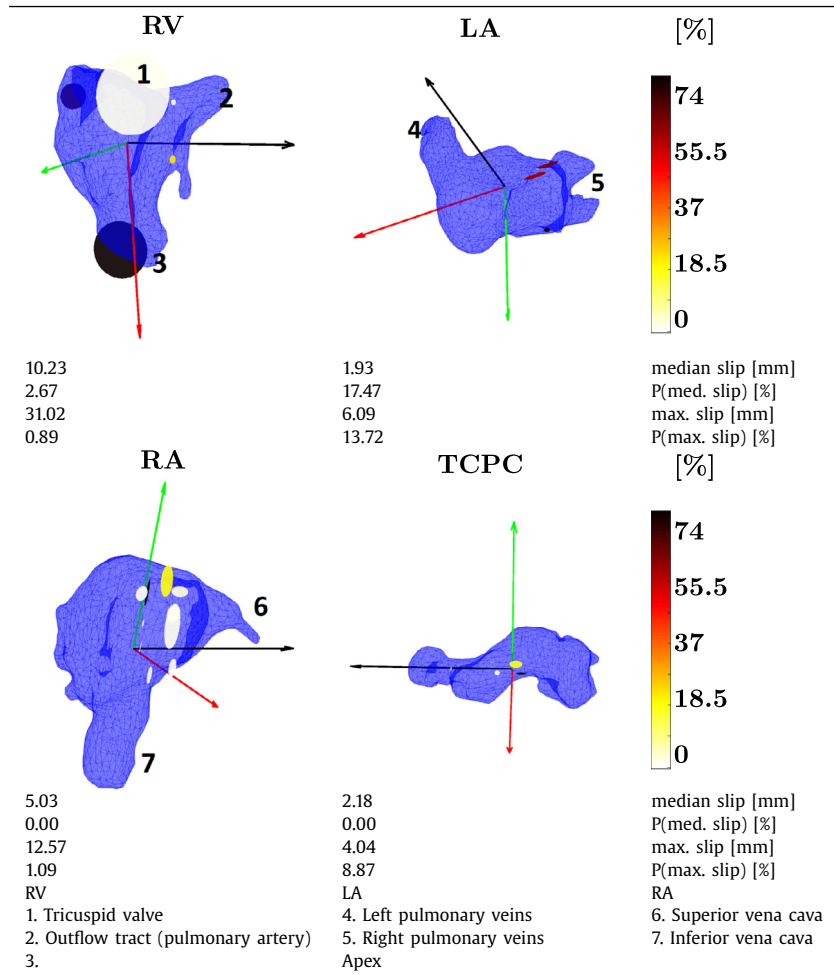


Fig. 11. Catheter tip slippage validation: (a) Histogram of coefficient values for the correlation of the decomposed 3D slippage with the 3D force values along the direction of the slippage. The 0.9 threshold showed a strong correlation for more than half of the points, while the 0.8 and 0.75 correlation coefficient values covered 66.30% and 70.74% of the points, respectively. (b) Correlation of slippage with contact force for different number of noise channels. The top of the bars represent the number of points within a certain interval of the correlation coefficient (black: 0.9–1, blue: 0.8–0.9, green: 0.75–0.8). The histogram in (a) is the detailed visualisation for 5 noise channels. (c) Example of 3D slippage curves (blue) and corresponding force components along the slippage direction (red). The correlation coefficients are -0.85 for the x-axis and 0.99 for the y and z-axes. The negative correlation shows opposite directions of the slippage and the force. (For interpretation of the references to colour in this figure legend, the reader is referred to the web version of this article.)

Table 2

Colour-coded probability maps of local slippage for CHD cases: RV, RA, LA, and TCPC. The maximal slippage at each mapping point is depicted as an ellipsoid with axis lengths corresponding to the Cartesian slippage components. The orientation of the surfaces is given by the left-right axis (black), superior-inferior axis (red), anterior-posterior axis (green).



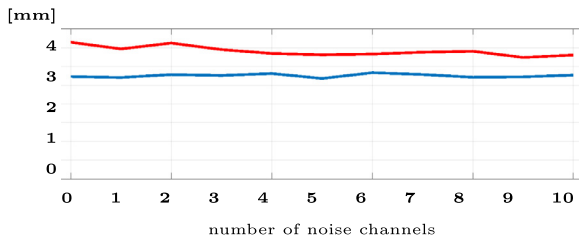


Fig. 12. Maximal slippage amplitudes in 2.5 s-long signals in ventricular (red) vs. atrial (blue) studies. According to clinical literature (Shah and Namdar, 2015), there tends to be worse contact and therefore more slippage in the ventricle compared to the atrium. There is no significant dependency on the number of noise channels, but there is a significant difference between atrial and ventricular studies (Wilcoxon rank sum test, 5% significance level). (For interpretation of the references to colour in this figure legend, the reader is referred to the web version of this article.)

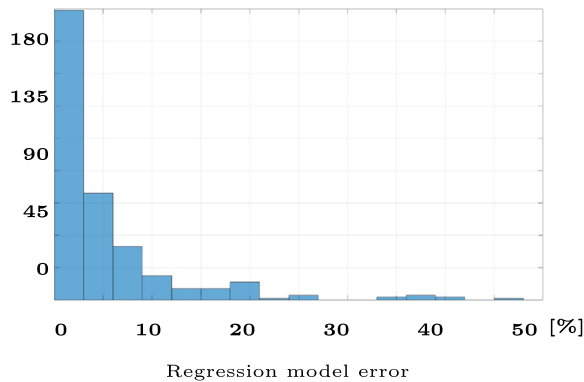


Fig. 13. Validation of the multivariate normal regression model used for generating the local probabilities in the DBN of each mapping point. The model was cross-validated 10 times for each point, with the test set comprising of a sliding window of 10% of the samples in the sequence and the training set covering the rest. The histogram shows the mean regression error over all validation tests at each mapping point.

While many multi-source signals are decomposed using band-pass filtering, PCA or ICA, it was shown that the short-length catheter signals can be better analysed using the data-driven MEMD. However, the convergence and stability of empirical methods cannot be studied in a conventional manner (Ahrabian and Mandic, 2015). Moreover, since there was no ground truth for either of the extracted signals other than the ECG, a series of quantitative and qualitative validation tests based on 3D contact force amplitude and orientation correlation and on qualitative analysis between anatomical groups were performed to demonstrate the results. Furthermore, tests on phantom and artificial data allowed for comparison with the other state-of-the-art decomposition algorithms.

The parameter of the proposed APIT-MEMD algorithm is the number of noise channels. An analysis on the influence of the number of noise channels was performed on several occasions (Figs. 10(b), 11(b) and 12). Apart from an outlier in the computation time of the method applied without any noise channels, it can be concluded that the computation time increases with the number of channels. In terms of performance, the differences are small. However, from a qualitative point of view, a number between 4 and 7 noise channels yielded good performance in both heart rate recovery (Fig. 10(b)) and in slippage correlation to the contact force amplitude and orientation (Fig. 11(b)).

The major challenge in the decomposition was the short data recording window of 2.5 ms for each mapping point. While the results of the empirical method were promising, it was difficult to extract the low-frequency respiratory wave from the short sequence. However, the phantom data experiments showed good ac-

curacy for longer sequences. Regarding the cardiac motion amplitude, the design of experiments currently assumed that the cardiac motion wave had the same frequency and amplitude in the pre-slippage and slippage time series. However, the catheter manipulation that simulated slippage was performed blindly under no control of the applied force and no visualisation of the resulting time series. Therefore, in several recordings, the effect of the catheter manipulation undermined the amplitudes of cardiac and respiratory motion and this caused a higher error in the amplitude recovery. With a force-sensing catheter and real-time visualisation of the position recording, the catheter manipulation can be performed more smoothly and the recovered amplitudes closer to the pre-manipulation values.

In accordance with (Shah and Namdar, 2015), the large amplitude of slippage compared to the other components proved that this effect should receive higher attention in catheter ablation procedures. In addition to its maximal value at each mapping point, the probability of this maximal drift was also assessed. Despite the submillimeter range of slippage in Figs. 11(c) and 12, the catheter drift becomes significant over prolonged periods of ablation. While the plotted values were extracted from 2.5 s-long sequences, the ablation of a single target normally takes 60 s, during which time the catheter tip slippage is incremental.

Multivariate normal regression was used to fit the slippage values at each time stamp to a mapping point-specific model with catheter tip positions and decomposed cardiac and respiratory motion as predictors. The regression errors were constrained to be normally distributed and thus assigned probabilities from a normal probability distribution function. The values were then mapped onto the corresponding slippage. Qualitative ground-truth of the slippage probability was inferred from clinical literature. One of the most unstable regions was confirmed by the proposed method as the pulmonary veins ostiae in the left atrium, as previously indicated in the clinical literature (Neuzil et al., 2013; Makimoto et al., 2014).

The contact force amplitude in the atrium was 187.99 ± 203.38 mN compared to 134.25 ± 176.02 mN in the ventricle, showing that it is more difficult to keep good contact in the ventricle. This is in accordance with the clinical observation of the larger motion range in the ventricle and the frequent loss of contact especially at diastole (Shah and Namdar, 2015). Prolonged loss of contact is more likely to cause sliding. We used this comparison between the atrium and ventricle to validate the amount of slippage in the two groups.

As demonstrated in the Results section, the shape of the slippage is significantly different than that of the cardiac or even the respiratory components. This is due to the assumption in the signal extraction, i.e., that slippage has a lower frequency than the other two components, and also due to the MEMD algorithm, which integrates potentially different components of the same frequency into a single IMF. Therefore, MEMD is unable to discriminate between cardiac motion and slippage or respiratory motion and slippage, if slippage has the same frequency as any of these two physiological motions. However, these cases would not be regarded as slippage, as this was defined in the Introduction as the relative drift to the cardiac wall. Since the cardiac wall is moving, only additional components build up the relative drift, i.e., slippage. The potential workflow integrating the proposed methods is depicted in Fig. 14. The catheter stability analysis is intended as a step of the electroanatomical mapping and can be performed simultaneously with the generation of the endocardial surface and of the electrical activation pattern. These two types of data are already incorporated in electroanatomical mapping systems and are based on sparse data acquisition at the mapping points locations. The catheter tip motion is readily acquired and can be used for online stability analysis. The resulting probability map can be used as an

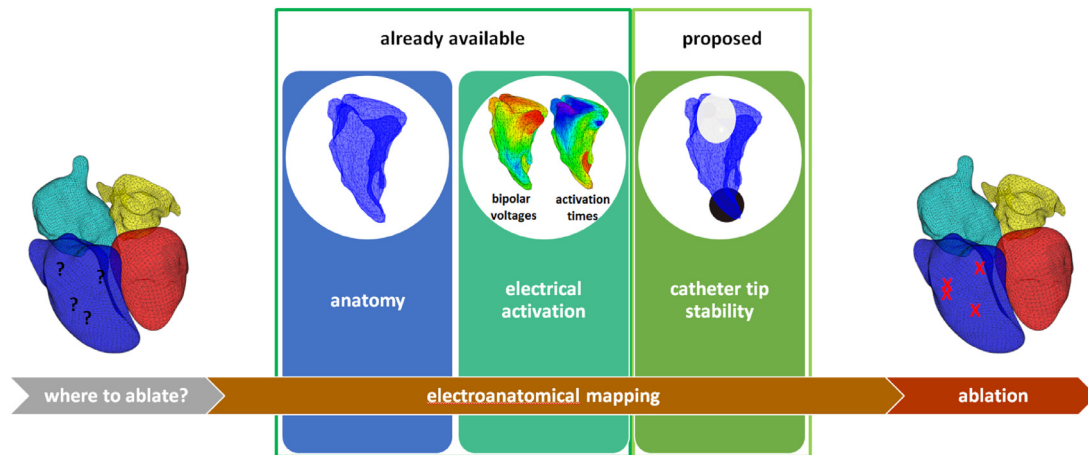


Fig. 14. Integration of the proposed methods into the clinical workflow of cardiac catheter ablation. Electrical activation and anatomy reconstruction are already performed simultaneously in all clinically used electroanatomical mapping systems. The information is gathered from sparse mapping points, for which the catheter tip position is also available. In this paper, the electroanatomical map is enhanced with this third step of catheter stability analysis from the tip motion data. The result is a slippage probability map, which adds to the anatomical and electrical activation data to aid the clinician in deciding the most stable ablation locations.

additional source of information for the decision on the optimal ablation locations.

5. Conclusion

Catheter tip stability is a prerequisite of successful cardiac ablation. Current electroanatomical mapping systems aid the clinician in visualising the complete cardiac activation, but there is no assessment of motion patterns at the targeted site. A new framework for intraoperative computer guidance based on catheter tip slippage measures and motion signal decomposition was proposed in this paper. With a combined information of the maximal 3D slippage and its probability, the clinician can decide on the ablation targets in order to find the stable positions to deliver RF energy or build a case for robotic navigation and stabilisation at difficult anatomical targets.

Finally, this work extends the results in (Constantinescu et al., 2015) and the presented analytical framework can be used for procedural planning in patients who require ablation in extremely unstable positions, but for whom alternative more stable neighbour sites can be found.

References

- Ahrbaban, A., Mandic, D.P., 2015. Selective time-frequency reassignment based on synchroqueezing. *IEEE Signal Process. Lett.* 22 (11), 2039–2043. doi:10.1109/LSP.2015.2456097.
- Cappato, R., Calkins, H., Chen, S.A., Davies, W., Iesaka, Y., Kalman, J., Kim, Y.H., Klein, G., Natale, A., Packer, D., Skanes, A., Ambrogi, F., Biganzoli, E., 2010. Updated worldwide survey on the methods, efficacy, and safety of catheter ablation for human atrial fibrillation. *Circ. Arrhythm Electrophysiol.* 3 (1), 32–38. doi:10.1161/CIRCEP.109.859116.
- Chugh, S.S., Havmoeller, R., Narayanan, K., Singh, D., Rienstra, M., Benjamin, E.J., Gillum, R.F., Kim, Y.H., McAnulty, J.H., Zheng, Z.J., Forouzanfar, M.H., Naghavi, M., Mensah, G.A., Ezzati, M., Murray, C.J., 2014. Worldwide epidemiology of atrial fibrillation: a global burden of disease 2010 study. *Circulation* 129 (8), 837–847. doi:10.1161/CIRCULATIONAHA.113.005119.
- Cignoni, P., Corsini, M., Ranzuglia, G., Meshlab: an open-source 3d mesh processing system. In: *ERCIM News*, pp. 45–46.
- Constantinescu, M., Lee, S.-L., Ernst, S., Yang, G.-Z., 2015. *Multi-source Motion Decoupling Ablation Catheter Guidance for Electrophysiology Procedures*. Springer International Publishing, Cham, pp. 213–220.
- Ernst, S., Babu-Narayan, S.V., Keegan, J., Horduna, I., Lyne, J., Till, J., Kilner, P.J., Pennell, D., Rigby, M.L., Gatzoulis, M.A., 2012. Remote-controlled magnetic navigation and ablation with 3d image integration as an alternative approach in patients with intra-atrial baffle anomaly. *Circ. Arrhythm Electrophysiol.* 5 (1), 131–139. doi:10.1161/CIRCEP.111.962993.
- Hemakom, A., Goverdovsky, V., Looney, D., Mandic, D.P., 2016. Adaptive-projection intrinsically transformed multivariate empirical mode decomposition in cooperative brain-computer interface applications. *Philos. Trans. A Math. Phys. Eng. Sci.* 374 (2065), 20150199. doi:10.1098/rsta.2015.0199.
- Hyvaerinen, A., Oja, E., 2000. Independent component analysis: algorithms and applications. *Neural Netw.* 13 (4–5), 411–430.
- King, A.P., Boubertakh, R., Rhode, K.S., Ma, Y.L., Chinchapatnam, P., Gao, G., Tangcharoen, T., Ginks, M., Cooklin, M., Gill, J.S., Hawkes, D.J., Razavi, R.S., Schaeffer, T., 2009. A subject-specific technique for respiratory motion correction in image-guided cardiac catheterisation procedures. *Med. Image Anal.* 13 (3), 419–431. doi:10.1016/j.media.2009.01.003.
- Klemm, H.U., Steven, D., Johnsen, C., Ventura, R., Rostock, T., Lutomsky, B., Risius, T., Meinertz, T., Willems, S., 2007. Catheter motion during atrial ablation due to the beating heart and respiration: impact on accuracy and spatial referencing in three-dimensional mapping. *Heart Rhythm* 4 (5), 587–592. doi:10.1016/j.hrthm.2007.01.016.
- Looney, D., Hemakom, A., Mandic, D.P., 2015. Intrinsic multi-scale analysis: a multivariate empirical mode decomposition framework. *Proc. Math. Phys. Eng. Sci.* 471 (2173), 20140709. doi:10.1098/rspa.2014.0709.
- Lujan, A.E., Larsen, E.W., Balter, J.M., Ten Haken, R.K., 1999. A method for incorporating organ motion due to breathing into 3d dose calculations. *Med. Phys.* 26 (5), 715–720. doi:10.1118/1.598577.
- Ma, Y., King, A.P., Gogin, N., Rinaldi, C.A., Gill, J., Razavi, R., Rhode, K.S., 2010. Real-Time Respiratory Motion Correction for Cardiac Electrophysiology Procedures Using Image-Based Coronary Sinus Catheter Tracking. *Springer Berlin Heidelberg*, Berlin, Heidelberg, pp. 391–399.
- Makimoto, H., Tilt, R.R., Lin, T., Rillig, A., Mathew, S., Deiss, S., Wissner, E., Metzner, A., Rausch, P., Bardyszewski, A., Zhang, Q., Kamioka, M., Leme, C., Kuck, K.H., Ouyang, F., 2014. Incidence and anatomical locations of catheter instability during circumferential pulmonary vein isolation using contact force. *Int. Heart J.* 55 (3), 249–255.
- Mandic, D.P., Rehman, N., Wu, Z., Huang, N.E., 2013. Empirical mode decomposition-based time-frequency analysis of multivariate signals: the power of adaptive data analysis. *IEEE Signal Process. Mag.* 30 (6), 74–86.
- Neuzil, P., Reddy, V.Y., Kautzner, J., Petru, J., Wichterle, D., Shah, D., Lambert, H., Yulzari, A., Wissner, E., Kuck, K.H., 2013. Electrical reconnection after pulmonary vein isolation is contingent on contact force during initial treatment: results from the efficacy i study. *Circ. Arrhythm Electrophysiol.* 6 (2), 327–333. doi:10.1161/CIRCEP.113.000374.
- Panayiotou, M., King, A.P., Ma, Y., Rinaldi, C.A., Gill, J., Cooklin, M., O’Neil, M., Rhode, K.S., 2012. Automatic image-based retrospective gating of interventional cardiac x-ray images. *Conf. Proc. IEEE Eng. Med. Biol. Soc.* 2012, 4970–4973. doi:10.1109/EMBC.2012.6347108.
- Porras, A.R., Piella, G., Berruzo, A., Hoogendoorn, C., Andreu, D., Fernandez-Armenta, J., Sitges, M., Frangi, A.F., 2013. Interventional endocardial motion estimation from electroanatomical mapping data: application to scar characterization. *IEEE Trans. Biomed. Eng.* 60 (5), 1217–1224. doi:10.1109/TBME.2012.2230327.
- Rehman, N., Mandic, D.P., 2010. Multivariate empirical mode decomposition. *Proc. R. Soc. Lond. A* 466 (2117), 1291–1302.
- Roujol, S., Anter, E., Josephson, M.E., Nezafat, R., 2013. Characterization of respiratory and cardiac motion from electro-anatomical mapping data for improved fusion of mri to left ventricular electrograms. *PLoS One* 8 (11), e78852. doi:10.1371/journal.pone.0078852.
- Roy, K., Gomez-Pulido, F., Ernst, S., 2016. Remote magnetic navigation for catheter ablation in patients with congenital heart disease: a review. *J. Cardiovasc. Electrophysiol.* 27 Suppl 1, S45–S56. doi:10.1111/jce.12903.
- Schmidt, R., Singh, K., 2010. Meshmixer: an interface for rapid mesh composition. In: *ACM SIGGRAPH 2010 Talks*, p. 6:1. doi:10.1145/1837026.1837034.

- Shah, D.C., Namdar, M., 2015. Real-time contact force measurement: a key parameter for controlling lesion creation with radiofrequency energy. *Circ. Arrhythm. Electrophysiol.* 8 (3), 713–721. doi:[10.1161/CIRCEP.115.002779](https://doi.org/10.1161/CIRCEP.115.002779).
- Squara, F., Latcu, D.G., Massaad, Y., Mahjoub, M., Bun, S.S., Saoudi, N., 2014. Contact force and force-time integral in atrial radiofrequency ablation predict transmural-ity of lesions. *Europace* 16 (5), 660–667. doi:[10.1093/europace/euu068](https://doi.org/10.1093/europace/euu068).
- Sundar, H., Khamene, A., Yatziv, L., Xu, C., 2009. Automatic image-based cardiac and respiratory cycle synchronization and gating of image sequences. *Med. Image Comput. Comput. Assist. Interv.* 12 (Pt 2), 381–388.
- Ur Rehman, N., Park, C., Huang, N.E., Mandic, D.P., 2013. Emd via memd: multivariate noise-aided computation of standard emd. *Adv. Adapt. Data Anal.* 05 (02), 1350007. doi:[10.1142/S1793536913500076](https://doi.org/10.1142/S1793536913500076).